Journal of Nuclear Materials 432 (2013) 205–211

Contents lists available at SciVerse ScienceDirect

Journal of Nuclear Materials

journal homepage: www.elsevier.com/locate/jnucmat

Understanding the phase equilibrium and irradiation effects in Fe–Zr diffusion couples

Chao-Chen Wei [a], Assel Aitkaliyeva [a,d], Zhiping Luo [a,b], Ashley Ewh [c], Y.H. Sohn [c], J.R. Kennedy [d], Bulent H. Sencer [d], M.T. Myers [e], M. Martin [e], J. Wallace [e], M.J. General [a], Lin Shao [a,e,*]

[a] Materials Science & Engineering Program, Texas A&M University, College Station, TX 77843, USA
[b] Microscopy and Imaging Center, Texas A&M University, College Station, TX 77843, USA
[c] Department of Materials Science and Engineering, University of Central Florida, Orlando, FL 32816, USA
[d] Fundamental Fuel Properties Department, Nuclear Fuel and Materials Division, Idaho National Laboratory, Idaho Falls, ID 83415, USA
[e] Department of Nuclear Engineering, Texas A&M University, College Station, TX 77843, USA

ARTICLE INFO

Article history:
Received 4 May 2012
Accepted 17 July 2012
Available online 26 July 2012

ABSTRACT

We have studied the radiation effects in Fe–Zr diffusion couples, formed by thermal annealing of a mechanically bonded binary system at 850 °C for 15 days. After irradiation with 3.5 MeV Fe ions at 600 °C, a cross sectional specimen was prepared by using a focused-ion-beam-based lift out technique and was characterized using scanning/transmission electron microscopy, selected-area diffraction and X-ray energy dispersive spectroscopy analyses. Comparison studies were performed in localized regions within and beyond the ion projected range and the following observations were obtained: (1) the interaction layer consists of $FeZr_3$, $FeZr_2$, Fe_2Zr, and $Fe_{23}Zr_6$; (2) large $Fe_{23}Zr_6$ particles with smaller core particles of Zr-rich Fe_2Zr are found within the α-Fe matrix; (3) Zr diffusion is significantly enhanced in the ion bombarded region, leading to the formation of an Fe–Zr compound; (4) grains located within the interaction layer are much smaller in the ion bombarded region and are associated with new crystal growth and nanocrystal formation; and (5) large α-Fe particles form on the surface of the Fe side, but the particles are limited to the region close to the interaction layer. These studies reveal the complexity of the interaction phase formation in an Fe–Zr binary system and the accelerated microstructural changes under irradiation.

1. Introduction

Zirconium metallurgy is of great importance in nuclear applications. Zr has a very low thermal neutron capture cross section. With optimized alloying for improved ductility and corrosion resistance, Zr-based alloys have been widely used as fuel cladding and other structural components for light water and pressurized water reactors. In Zircaloy-2, which is used as fuel cladding in boiling water reactors, Zr is alloyed with 1.2–1.7 wt.% Sn, 0.07–0.2 wt.% Fe, and other metals including Cr and Ni. Zircaloy-4, whose Fe addition is slightly increased to 0.18–0.24 wt.% Fe in comparison with Zircolay-2, is used for pressurized water reactors [1]. Although the Fe composition range in Zircaloy alloys is relatively low, understanding the Fe–Zr interaction is important for evaluating reactor safety, and in particular, for the joining region between Zircaloy and low cost structural components comprised of carbon steels. Furthermore, Fe–Zr alloys, e.g. stainless steel-15 wt.% Zr and Zr-8 wt.% stainless steel, have been considered as potential waste forms [2]. In addition, information regarding interactions between Fe and Zr is important for fuel clad chemical interaction studies for fast reactors.

Fig. 1 shows a phase diagram which is supported by the results of the present study [3]. From high to low Zr concentration, equilibrium phases include $FeZr_3$, $FeZr_2$, Fe_2Zr, and $Fe_{23}Zr_6$. A quick summary of each phase from the recent systematic investigation is provided for reference: (1) $FeZr_3$ has a Re_3B-type orthorhombic structure and exists at a composition range of 74.8–75.4 at.% Zr (experimentally determined at temperatures ⩽851 °C); (2) $FeZr_2$ has a $CuAl_2$-type tetragonal structure at low temperature, a Ti_2Ni-type structure at high temperature, and exists at a composition of approximately 67 at.% Zr; (3) Fe_2Zr has a $MgCu_2$-type face-centered cubic structure, which has a slightly increasing lattice constant with increasing Zr content and starts transforming to a hexagonal structure above 1230 °C [4], and exists at a composition range of 27.5–34.4 at.% Zr; and (4) $Fe_{23}Zr_6$ has a Th_6Mn_{23}-type structure [4].

* Corresponding author at: Department of Nuclear Engineering, Texas A&M University, College Station, TX 77843, USA. Tel.: +1 979 845 4107; fax: +1 979 845 6443.
E-mail address: lshao@tamu.edu (L. Shao).

0022-3115/$ - see front matter © 2012 Elsevier B.V. All rights reserved.
http://dx.doi.org/10.1016/j.jnucmat.2012.07.027

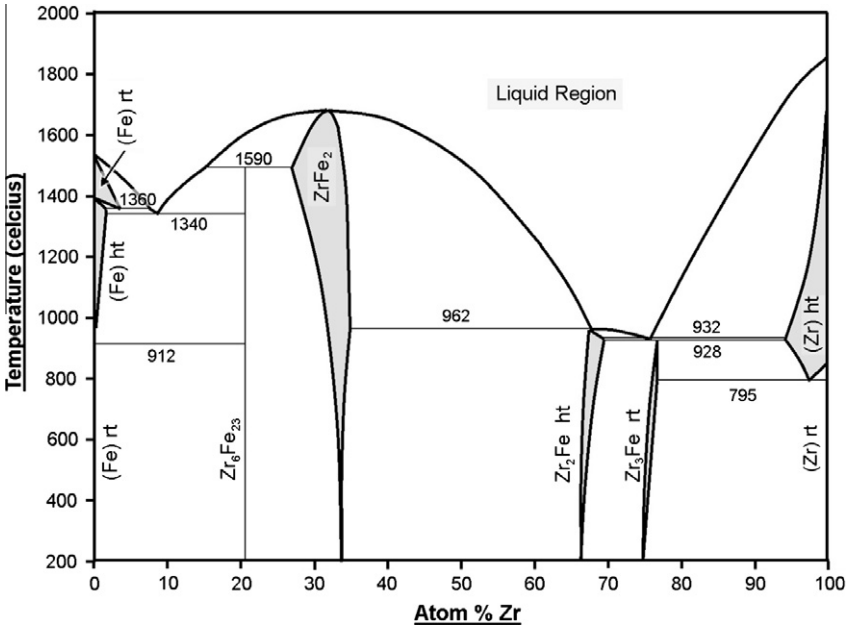

Fig. 1. Phase diagram of Fe–Zr (adopted from Jiang [3]).

Although technologically important, the Fe–Zr system is not completely understood. Contradictions exist regarding the nature of the $FeZr_2$ and $Fe_{23}Zr_6$ phases. For example, $Fe_{23}Zr_6$ is reported to be an equilibrium phase in the diagrams proposed by Kubaschewski [5] and Arias and Abriata [6], but not in those introduced by Alekseeva and Korotkova [7] and Stein et al. [4]. Previous studies have suggested that it is either a high temperature phase or a phase stabilized by impurities or contamination from crucible materials [4]. It has also been argued that both $FeZr_2$ and $Fe_{23}Zr_6$ are oxygen stabilized and neither belongs to the equilibrium phase diagram. Even in those studies, which suggest that $Fe_{23}Zr_6$ belongs to the equilibrium phase diagram, the phase formation mechanism has been debated. Liu et al. observed nucleation of $Fe_{23}Zr_6$ on the surface of Fe_2Zr particles and proposed a peritectoid reaction (α-Fe) + $Fe_2Zr \leftrightarrow Fe_{23}Zr_6$ [8]. In contrast, Abraham et al. noticed α-Zr formation within the $Fe_{23}Zr_6$ phase and proposed a two-step growth mechanism: Fe_2Zr first transforms into $Fe_{23}Zr_6$ + α-Zr, where α-Zr subsequently reacts with α-Fe to form more $Fe_{23}Zr_6$ [9].

In an effort to understand phase equilibrium in the Fe–Zr system and to investigate radiation effects on the interaction compound formation, Fe–Zr diffusion couples formed by thermal interdiffusion of Fe and Zr were studied. The diffusion couple method does not restrict the formation of any of the phases allowed in the phase diagram when the system is at thermodynamic equilibrium. This avoids the complexity of testing a large alloying matrix with various ratios of Fe–Zr, which is often the case in traditional alloying approaches. Intermetallic compounds formed in a binary system are often brittle and thus, generally have low radiation tolerance. Mechanical failure such as cracking can develop under neutron irradiation and can cause serious reactor safety issues [10]. In a diffusion couple, the radiation response of each intermetallic compound phase can be compared with the regions beyond the ion penetration range. Due to the fragility of the irradiated diffusion couple, conventional sample preparation method, based on ion milling technique, is difficult to prepare cross-sectional TEM specimens. Therefore, a focused ion beam (FIB)-based lift out technique was used to prepare specimens for atomic scale characterization of structural changes along and well beyond the ion penetration depth.

2. Experimental procedure

An Fe–Zr diffusion couple was fabricated by furnace annealing in vacuum at a temperature of 850 °C for 15 days. The couple, made by mechanical bonding of two polished, polycrystalline Fe (99.99%) and Zr (99.2%) metal disks, was sealed inside a quartz capsule using an oxy-propane torch. Prior to sealing, the capsule was repeatedly pumped and purged with both argon and hydrogen gas to reach a vacuum better than 10^{-6} torr. The residual gas, the mixture of argon and hydrogen, is helpful to reduce oxidation, due to preferred chemical bonding between hydrogen and oxygen.

At the end of annealing, the capsule was dropped into cold water and immediately sacrificed using a hammer to accelerate quenching. The formed diffusion couple was then irradiated in a 1.7 MeV tandetron accelerator with 3.5 MeV Fe ions to 3.5×10^{16} Fe/cm^2 to create ~130 dpa (displacements per atom) at the damage peak at a temperature of 600 ± 10 °C in a vacuum better than 10^{-6} torr. The depth profiles of Fe implants and displacements per atom, both obtained from SRIM calculations [11], are provided in Fig. 2. The beam was scanned over a region of about 1 cm^2 with an average beam current of 270 nA/cm^2. The sample temperature was measured using a thermocouple mounted on the substrate holder which was self adjusted by a feedback system with an overall temperature fluctuation of less than 20 °C.

After ion irradiation, cross-sectional TEM specimens were prepared in a FEI Quanta 3D FEG dual beam SEM/FIB microscope using a lift out technique. Final specimen dimensions were 20 μm × 13 μm × 70 nm (width × height × thickness). The specimen surface and ion irradiation induced features were protected from Ga^+ ion beam damage in the FIB with a platinum strip. The damage on the cross-sectional sides of TEM specimens was minimized due to Ga^+ ion bombardment at a glancing angle. The bombardment consisted of two steps. The first step used relatively large Ga^+ beam currents for quick material removal and the second step used a low current beam for fine cutting and further specimen thinning. Microstructural characterization and elemental mapping were performed in the same microscope using a 30 kV electron beam. The thinner region was characterized using two transmission electron microscopes, a JEOL JEM-2010 and a FEI TECNAI G2

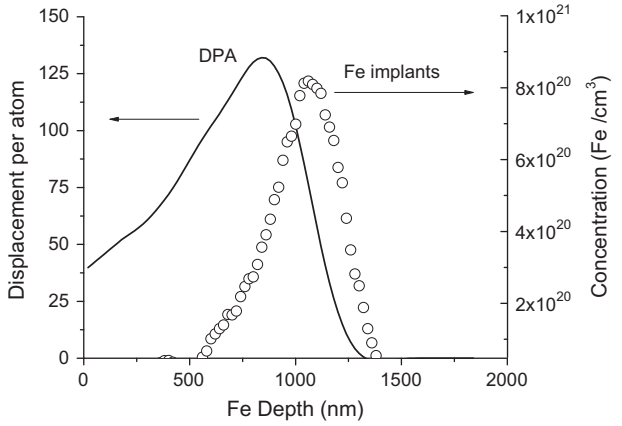

Fig. 2. Depth profiles of Fe implants and displacements per atom ratios in 3.5 MeV Fe^{++} ion irradiated Fe.

F20 ST, both operated at an accelerating voltage of 200 kV. Bright and dark-field imaging, scanning TEM (STEM) imaging using a high-angle annular dark field (HAADF) detector, selected area diffraction (SAD) and nanobeam X-ray energy dispersive spectroscopy (EDS) analyses were preformed to characterize microstructures and microchemistry of the specimen. It should be mentioned that in the TEM mode, the contrast of a conventional resolution image is controlled by the mass-thickness (Zr appears darker than Fe), as well as the diffraction contrast (a grain near the Bragg diffraction condition with more diffracted intensity shows a darker contrast over a grain with less diffracted intensity). However in the HAADF STEM mode, the image contrast is controlled by the mass-thickness only, or *Z*-contrast.

3. Results and discussion

Fig. 3a shows a SEM micrograph of the diffusion couple after ion irradiation. The surface topography features a micro-crack along the original Fe–Zr interface and high-density island/particle formation. Fig. 3b is the corresponding Fe mapping which reveals that the particles form only on the Fe side of the interface. Such islands/particles were not observed in the sample before ion irradiation and thus, are not a result of phase segregation predicted in the phase diagram. At a depth beyond the ion irradiated region, no such particles were found. This suggests that the particle formation was caused by irradiation enhanced Zr diffusion near/on the surface.

The presence of the particles causes large signal fluctuations and shields compositional information beneath the surface due to the large electron-specimen interaction volume in SEM analysis. Therefore, further characterization was performed via TEM. Fig. 4 shows the STEM micrograph obtained from the cross sectional specimen of the ion irradiated sample. The gray arrow refers to the Pt strip deposited for surface protection. The left side of the micrograph with lighter contrast corresponds to the Zr side and the right side with relatively darker contrast corresponds to the Fe side. The interaction layer in the middle contains particles of irregular shapes/patterns and suggests the existence of multiple phases. The bracket on the right side marks the ion irradiated region which is approximately 1.3 μm beneath the surface. For comparison, EDS line scanning was performed at a depth well beyond the ion bombardment region (denoted by the solid line) and at a depth within the ion irradiated region (denoted by the dash line).

Fig. 5a displays a plot of the Fe and Zr composition changes across the interface. This spectrum was collected from the region indicated by the solid line as shown in Fig. 4. The vertical dash line refers to the original Fe–Zr interface. Both distributions of Zr in Fe

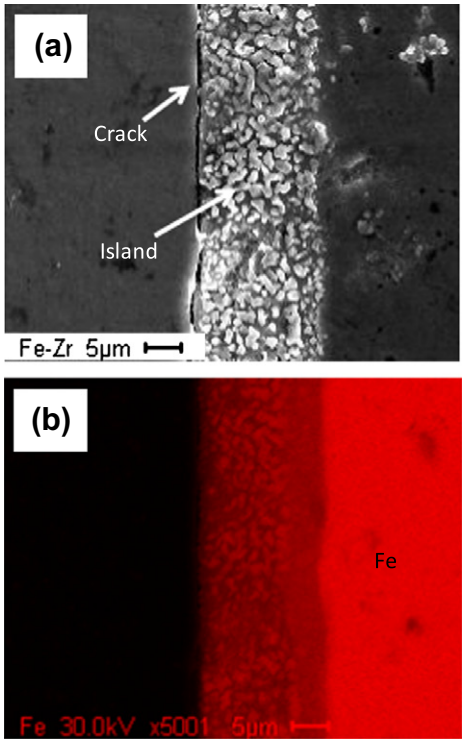

Fig. 3. (a) SEM micrograph of the Fe–Zr sample after irradiation and (b) corresponding Fe map.

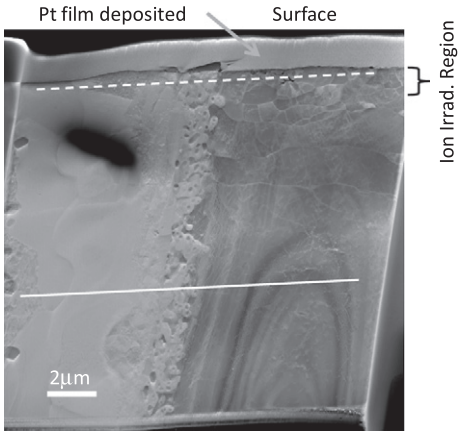

Fig. 4. STEM micrograph obtained from cross sectional specimen of the ion irradiated Fe–Zr diffusion couple.

and Fe in Zr show step-like profiles. This can be understood from the Gibbs phase rule in which the degrees of freedom are described as $F = C - P + 2$, where C is the number of components, and P is the number of phases [12]. In an Fe–Zr binary system, when the composition corresponds to the co-existence of two phases in the phase diagram, $C = 2$, $P = 2$, and $F = 2$. Under given pressure and temperature, there is no additional freedom for composition changes, which leads to a step distribution. For each step height, corresponding to a single phase in a phase diagram, the composition is allowed to vary within stoichiometric region. This can be derived from the phase diagram since $P = 1$ and $F = 3$. As shown in Fig. 5a, compositional analysis suggests that steps A, B, and C correspond to $FeZr_3$ (74.4 at.% Zr), $FeZr_2$ (66.9 at.% Zr), Fe_2Zr (32.2 at.% Zr), respectively. Complexity arises for step D which contains a mixture of multiple phases including α-Fe, Fe_2Zr, and $Fe_{23}Zr_6$ (to be discussed later).

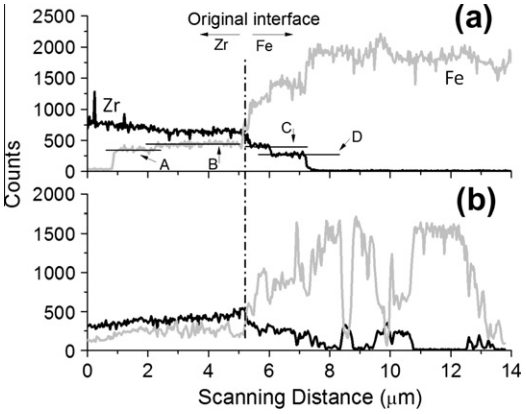

Fig. 5. Zr and Fe profiles across the interface obtained from STEM EDS line scanning.

For a comparison, Fig. 5b shows the Fe and Zr composition profiles from the ion irradiated region. The scan was performed at a depth of less than 0.5 μm beneath the sample surface. No step distributions were observed and diffusion is abnormally enhanced when compared to the scan acquired far below the irradiated region (Fig. 5a). Zr signals appear at a distance of approximately 8 μm away from the interface. As shown in Fig. 5a, Zr diffusion ends with the $Fe_{23}Zr_6$ phase (mixed with Fe_2Zr and Fe) at a distance of ~2 μm from the interface. Furthermore, both the Zr and Fe profiles contain large fluctuations in the irradiated region. Careful comparison with corresponding STEM micrographs indicates that the fluctuations occurred when the line scan encountered either newly precipitated particles or large grain boundaries. These observations suggest that atomic migration is enhanced under ion irradiation through grain boundary diffusion.

Correlated TEM images are overlapped in Fig. 6 to show microstructural changes of the interaction layer after ion bombardment. The dash line refers to the original Fe–Zr interface and the solid line refers to the projected range (R_p) of 3.5 MeV Fe ions, which is

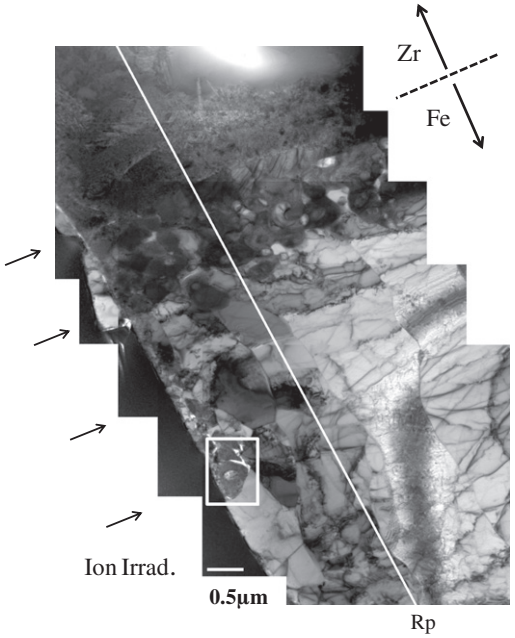

Fig. 6. Combination of series of bright-field TEM micrographs obtained from the ion irradiated diffusion couple. Arrows refer to the ion irradiation direction and the white solid line denotes the projected range of 3.5 MeV Fe ions. The dash line marks the original Fe–Zr interface.

~1.1 μm beneath the sample surface. Smaller grains with dark contrast appear within ~1 μm from the interface within the ion irradiated region. The dark contrast is possible due to either the presence of Zr within the grains, or diffraction contrast from satisfying the Bragg diffraction condition. Based on line scanning results, we believe that the dark contrast is caused by enhanced Zr migration under ion irradiation, and the subsequent formation of small particles of Fe–Zr phases. This process is accompanied with grain refinement.

Fig. 7a shows a bright-field TEM micrograph of regions near the surface and the interface. The dash line refers to the original Fe–Zr interface. No sharp or smooth phase interfaces were observed. Instead, particles of dark contrast penetrated into the Fe side, forming irregular interfaces. These particles, according to both diffraction analysis and localized EDS composition analysis, were determined to be primarily $Fe_{23}Zr_6$, while some were identified as Fe_2Zr. Fig. 7b shows an enlarged micrograph corresponding to the white box in Fig. 7a where points A through E refer to locations at which SAD analysis was conducted. For the region beyond the ion projected range, diffraction patterns confirm the existence of α-Fe (point A) and $Fe_{23}Zr_6$ (point B). Arrows mark the expected diffractions from the database. Both $Fe_{23}Zr_6$ (point C) and Fe_2Zr (point D) phases were identified within the ion penetrated region. SAD of point E clearly shows ring-like features, which suggests much smaller grains. Such ring-like features were observed in SAD patterns of different phases when the analyzed regions were located within the ion projected range region, which suggests that nanocrystal formation and grain refinement are caused by irradiation.

Fig. 8 shows a STEM micrograph obtained from the interaction region. It shows that gray particles form in the dark matrix. Within the gray particles, dark core particles are clearly visible. These dark core particles appear only inside the gray particles, and never appear on the boundary of the gray particles and dark matrix. Fig. 9 shows corresponding at.% composition profiles obtained from X-ray energy dispersive (EDX) line scanning microanalysis with a beam spot size of ~1 nm in the STEM mode, following the dash line in Fig. 8. The composition profiles suggest the following phases: (a) the dark matrix is Fe; (b) the large, light gray particles are $Fe_{23}Zr_6$; and (c) the smaller, dark particles inside $Fe_{23}Zr_6$ are O-rich Fe_2Zr phase. The Zr composition in the $Fe_{23}Zr_6$ phase is measured to be 20 at.%. If absorbed oxygen is assumed to take Zr substitutional sites, an oxygen-free phase expects to have Zr composition 25 at.%, which agrees with the composition range measured by Liu et al. [8]. As for the Zr-rich dark core particles, the Zr composition is about 40 at.%. Even considering that 30 at.% O consumes 15 at.% Zr to form ZrO_2, the remaining composition is 25Zr–30Fe. This deviates from all known composition ranges of stable phases. Furthermore, the dark particle on the left side has lower Fe content, but higher O content than the one on the right side. However, the sum of the Fe and O signals remains constant at about 60%, which suggests that oxygen may take the original Fe lattice sites. This finding suggests that, at least when compared with the core particles and Fe matrix, the $Fe_{23}Zr_6$ phase is not a phase which strongly absorbs oxygen.

The $Fe_{23}Zr_6$ phase observed from the present study is found to always surround Zr-rich core particles. Therefore, the following mechanism is proposed: the $Fe_{23}Zr_6$ phase starts to form at the original Fe_2Zr–(α-Fe) interface through the peritectoid reaction (α-Fe) + $Fe_2Zr \leftrightarrow Fe_{23}Zr_6$ proposed first by Liu et al. [8]. If continuous Fe diffusion from the α-Fe matrix and through the Fe_3Zr phase shell becomes difficult for inside growth of the $Fe_{23}Zr_6$ phase, the required Fe atoms for transformation are compensated through Fe diffusion from inside the Fe_2Zr phase. One consequence of this is Fe depletion of the Fe_2Zr core particle within the $Fe_{23}Zr_6$ phase. If Fe depletion reaches a significant level, it is possible that Fe_2Zr transforms into an equilibrium phase predicted at low-Fe wt.%

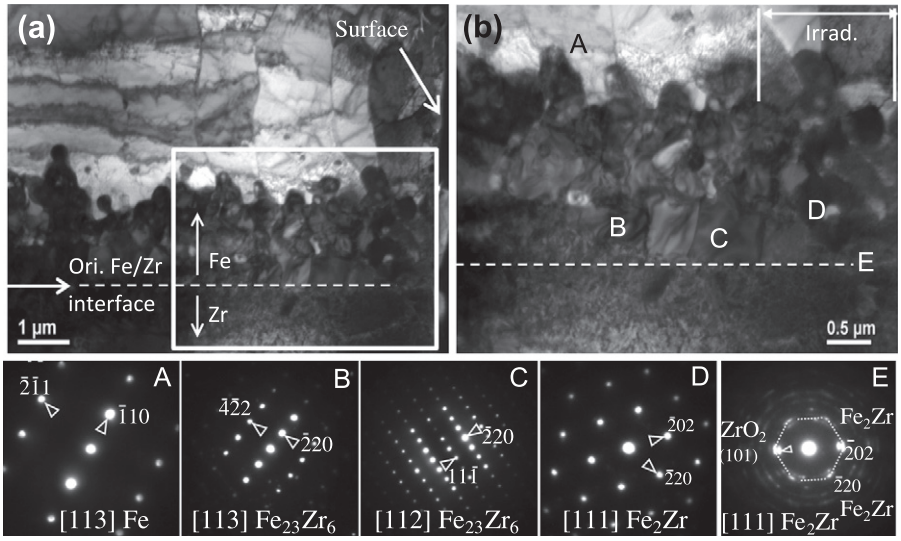

Fig. 7. (a) Bright-field TEM micrograph obtained from the ion irradiated diffusion couple and (b) enlarged bright-field TEM micrograph obtained from the white box marked in (a). SAD patterns for points A–E marked in (b) are shown for comparison. The dash lines in both (a) and (b) refer to the original Fe–Zr interface.

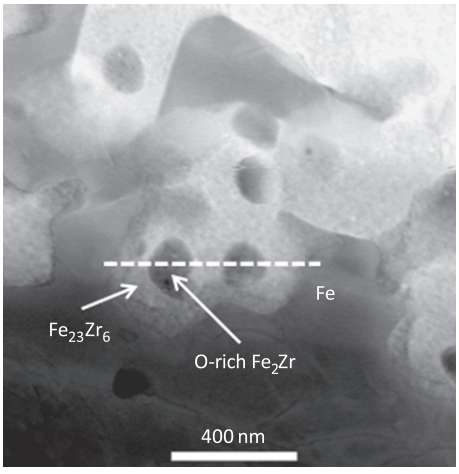

Fig. 8. The STEM micrograph obtained from the interaction region containing Fe_3Zr particles surrounding Zr-rich core. The line refers to the line scanning for EDX analysis.

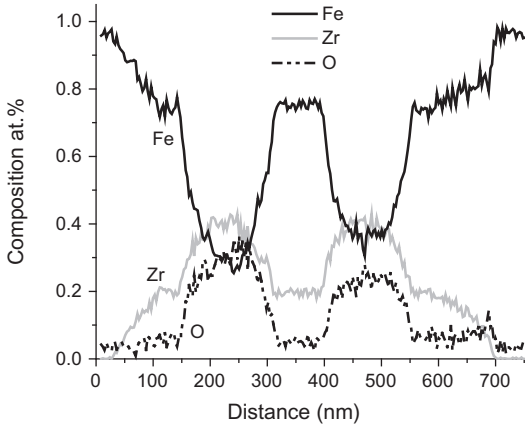

Fig. 9. Elemental mapping of Fe, Zr, and O obtained from EDX line scanning along the solid line specified in Fig. 8.

regions of the Fe–Zr phase diagram. This might be one possible explanation for finding the α-Zr and Fe–Zr mixture within $Fe_{23}Zr_6$ phase, as previously observed by Abraham et al. [9]. Therefore, although Abraham et al. argued an $Fe_{23}Zr_6$ formation mechanism different from that suggested by Liu et al., it is likely that their observation was a result of the subsequent transformation of Fe-depleted Fe_2Zr after the first step of the transformation proposed by Liu et al.

Previous studies have reported that the $Fe_{23}Zr_6$ phase always contains a significant amount of oxygen. Thus, it was determined to be a metastable phase that requires oxygen for phase stabilization [4]. However, it remains questionable whether the spatial resolution of a few microns in elemental mapping is fine enough to differentiate a possible localized mixture of $Fe_{23}Zr_6$ and other oxygen-rich phases. As shown in Fig. 8, this study indicates that the Fe_2Zr core particle, instead of $Fe_{23}Zr_6$, has strong oxygen absorption. These oxygen atoms may originally come from surface contamination prior to mechanical bonding. Additional oxygen absorption could also occur after/during TEM specimen preparation. Since oxygen atoms take Fe substitutional sites, the oxygen absorption and oxide formation can be attributed to the Fe vacancy enrichment, the consequence of Fe diffusion from Fe_2Zr to $Fe_{23}Zr_6$.

Fig. 10a–c further reveal microstructures of the $Fe_{23}Zr_6$ surrounded particles. The box in Fig. 10a (STEM image) is used to specify the characterization region in which a dark core is enclosed within a gray $Fe_{23}Zr_6$ particle. The box region was further characterized by switching from STEM to TEM mode. Fig. 10b shows SAD analysis of the dark core within the box. The lattice distances determined from the SAD analysis suggest that the core particle is a mixture of ZrO_2 and Fe_2Zr. The ring-like diffraction patterns further suggest that the core particle consists of small grains. This agrees with the dark field TEM micrograph shown in Fig. 10c. The white spots are nanometer size oxide particles formed in the core region. No such nanocrystals were observed in the surrounding $Fe_{23}Zr_6$ phase region.

Fig. 11 is the bright field TEM micrograph also from the region specified by the box in Fig. 10a. Dislocations are found to emit from the core particle. Furthermore, inside the core particle, dislocations of even higher densities are formed in the outermost shell. The defects can be induced by two factors: (1) one is a high defect density (vacancies) due to Fe depletion and (2) the existence of stress fields

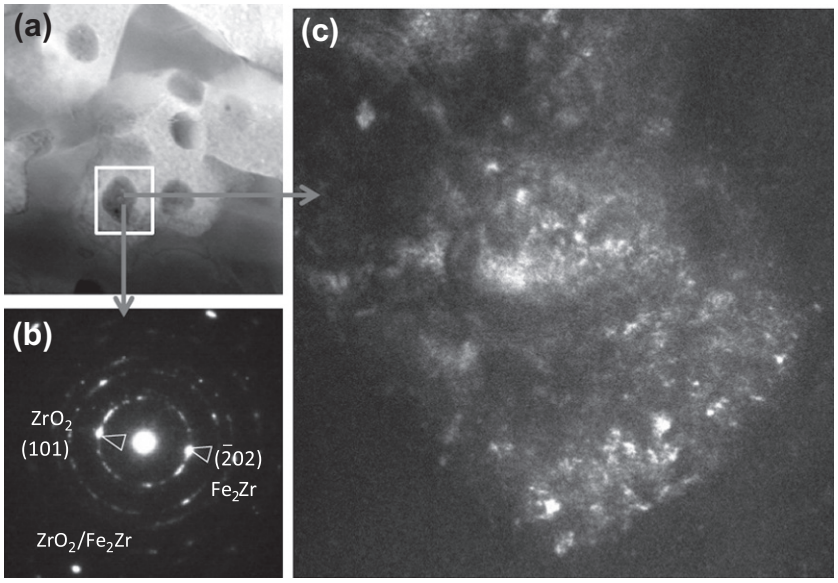

Fig. 10. (a) STEM micrograph of one selected interaction region; (b) SAD pattern obtained from the core particle within the box specified region in (a); and (c) dark field TEM micrograph from the same region.

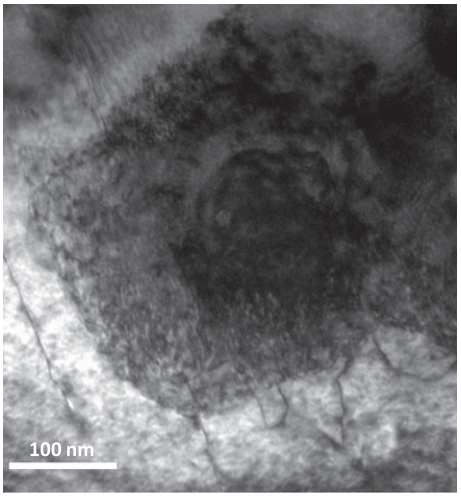

Fig. 11. Bright filed image TEM micrograph obtained from the region specified by the box in Fig. 10a.

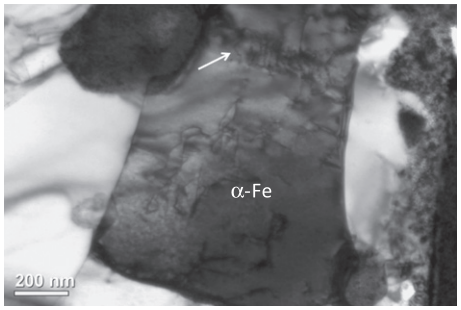

Fig. 12. Bright-field TEM micrograph obtained from the ion irradiated region of the diffusion couple.

at the phase boundaries. It is worthwhile to note that Figs. 10 and 11 were obtained from a depth beyond the ion penetration region. Therefore, the observed phase formation and dislocation formation were not a result of ion irradiation. On the other hand, similar features were observed even within the ion irradiated region. For example, the box in Fig. 6 refers to a near surface $Fe_{23}Zr_6$ particle having an oxygen rich Fe_2Zr core.

As for the defect development within the irradiated regions, Fig. 12 shows a typical bright-field TEM micrograph from the near surface region. The particle with relatively dark contrast in the center, which was determined by SAD analysis to be α-Fe, contains dislocations. Although dislocations were also observed at depths well beyond the ion irradiated region, fewer dislocations were observed in unirradiated regions. Thus, we can conclude that the dislocations observed in Fig. 12 were primarily caused by ion irradiation. A fraction of these dislocations undergo migration at elevated temperature, leading to elongation and pulling out, and the formation of dislocation networks. As marked by the arrow, the domain also consists of dislocations piled up along a band-like channel. The dislocation pile up is possibly caused by dislocation injection from a highly stressed region which is induced by the particle of dark contrast on the top-left side of Fig. 12.

The high density of large sized particles that covered the surface of the Fe side only, as shown in the SEM micrograph in Fig. 3a, were further characterized via TEM. Fig. 13a shows a bright-field TEM micrograph where the arrow refers to one of the surface particles. Fig. 13b–d are SAD patterns collected from the particle under different electron beam orientations, and Fig. 13e is a convergent beam electron diffraction pattern along [1 1 1] orientation exhibiting its cubic symmetry. These diffraction peaks all agree well with database for α-Fe. The diffraction patterns also exhibit ring-like features suggesting that the particle is polycrystalline with nanometer sized grains.

As shown in Fig. 13a, the particle remains on the top of a smooth surface. It is unlikely that the particle formed due to bulk phase segregation or simply pulled out from the bulk due to grain migration. This is due to the fact that these two mechanisms would lead to a very rough interface between the particle and the substrate. Since the particles were not observed prior to ion irradiation, it can be concluded that their formation results from crystal growth with enhanced Fe migration on the surface. Such growth is expected to be athermal due to energy transfer under ion bombardment conditions. The particle formation was limited to the region within 15 μm from the interface. Thus, it must be relevant to microstructural and compositional changes in the interaction

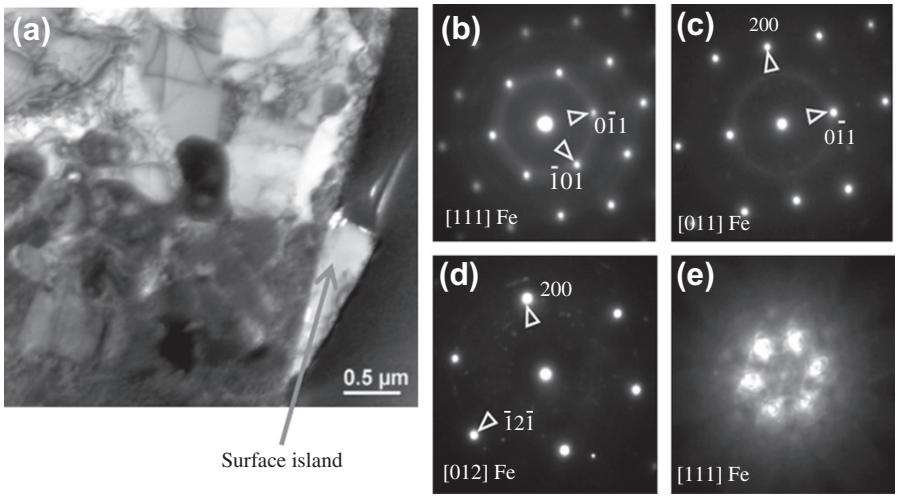

Fig. 13. (a) Bright-field TEM micrograph obtained from the irradiated sample and (b–e) SAD patterns collected under different orientations for the surface particle marked by the arrow in (a).

layer. Fe–Zr phase formation and grain refinement may provide additional driving forces and boundary diffusion paths for Fe migration towards the surface and promote crystal nucleation and growth. The exact mechanism, however, remains unclear.

4. Conclusion

In summary, the present experimental study shows the complexity of interaction compound formation in the Fe–Zr system. The study also sheds light on the formation mechanism of the $Fe_{23}Zr_6$ phase and suggests a phase transformation path from Fe_2Zr to $Fe_{23}Zr_6$ based on the finding that core particles of Zr rich Fe_2Zr form within large $Fe_{23}Zr_6$ particles. Comparison studies between regions with and without damage caused by high energy Fe ion irradiation show that radiation damage can accelerate Zr and Fe interdiffusion and can consequently cause significant microstructural and compositional changes. Zr atoms diffuse along the grain boundaries, penetrate deeply into the Fe side, and induce Fe–Zr phase formation, which leads to grain refinement. At the interaction layer and on the Fe side, large particles of α-Fe phase form as a result of Fe diffusion and surface crystal nucleation and growth, which are all enhanced by ion bombardment.

Because a diffusion couple can form phases across a wide range of compositions it can be used for fundamental studies. Combined with ion irradiation, the approach can be applied to understand the radiation tolerance of different phases, thus proving useful for the development of base alloys for reactor applications. The joining region between components of different metals requires a full-scale evaluation within a radiation environment. The microstructural changes and compound formation in the joining region, in addition to ion irradiation, high temperature, and corrosive environment, may eventually lead to accelerated cracking and structural failure.

Acknowledgement

This work was supported by the US Department of Energy under DOE-NE Idaho Operations Office Contract DE-AC07-05ID14517.

References

[1] C. Lemaignan, A.T. Motta, Zirconium Alloys in Nuclear Applications, Materials Science and Technology, Wiley-VCH, New York, 2006. pp. x–y.
[2] S.M. McDeavitt, D.P. Abraham, D.D. Keiser Jr., and J.Y. Park, in: Proceedings Conference SPECTRUM'96, Seattle, Washington, vol. 2477, 1996.
[3] M. Jiang, J. Phase Equilib. 22 (2001) 406.
[4] F. Stein, G. Sauthoff, M. Palm, J. Phase Equilib. 23 (2002) 480.
[5] O. Kubaschewski, Iron—Binary Phase Diagrams, Springer-Verlag, Berlin, Germany, 1982. pp. 175–178.
[6] D. Arias, J.P. Abriata, Bull. Alloy Phase Diagrams 9 (1988) 597.
[7] Z.M. Alekseeva, N.V. Korotkova, Russ. Metall. 4 (1989) 197.
[8] Y.P. Liu, S.M. Allen, J.D. Livingson, Scr. Metall. Mater. 32 (1995) 1129.
[9] D.P. Abraham, J.W. Richardson Jr., S.M. McDeavitt, Scr. Mater. 37 (1997) 239.
[10] Gary S. Was, Fundamentals of Radiation Materials Science: Metals and Alloys, Springer, New York, 2007. pp. 765–790.
[11] J.F. Ziegler, J.P. Biersack, M.D. Ziegler, The Stopping and Range of Ions in Matter, Lulu Press Co., Norrisville, NC, USA, 2009.
[12] J.W. Gibbs, The Scientific Papers of J. Willard Gibbs, Dover Publications, Inc., New York, 1961.